Transient buoyancy-driven front dynamics in nearly horizontal tubes

T. Séon, J. Znaien, D. Salin, and J. P. Hulin
Laboratoire Fluides, Automatique et Systèmes Thermiques, UMR No. 7608, CNRS, Université Paris 6 and 11, Bâtiment 502, Université Paris Sud, 91405 Orsay Cedex, France

E. J. Hinch
DAMTP-CMS, University of Cambridge, Wilberforce Road, CB3-OWA Cambridge, United Kingdom

B. Perrin
Laboratoire Pierre Aigrain, UMR 8551, CNRS, Ecole Normale Supérieure, Département de Physique, 24 rue Lhomond, 75231 Paris Cedex 05, France

(Received 11 May 2007; accepted 22 October 2007; published online 10 December 2007)

The interpenetration of light and heavy liquids has been studied in a long tube inclined at small angles α to the horizontal. For angles greater than a critical angle α_c (whose value decreases when the density contrast measured by the Atwood number At increases), the velocity of the interpenetration front is controlled by inertia and takes the steady value $V_f = k_i(\mathrm{At}\, gd)^{1/2}$, with $k_i \simeq 0.7$. At lower angles, the front is initially controlled by inertia, but later limited by viscous effects. The transition occurs at a distance X_{fc}, which increases indefinitely as α increases to α_c. Once the viscous effects act, the velocity of the front decreases in time to a steady value V_f^∞ which is proportional to sin α. For a horizontal tube in the viscous regime, the velocity of the front decreases to zero as $t^{-1/2}$. At the same time, the profile of the interface $h(x,t)$ only depends on the reduced variable $x/t^{1/2}$. A quasi-unidirectional model reproduces well the variation of the velocity of the front and the profiles of the interface, both in inclined and horizontal tubes. In the inclined tube, the velocity of the front is determined by matching rarefaction waves to a shock wave. © *2007 American Institute of Physics*. [DOI: 10.1063/1.2813581]

I. INTRODUCTION

Buoyancy-driven flows of a light fluid displacing a heavier one, or gravity currents of a heavy fluid over a surface, often occur in oceanography, meteorology, and chemical engineering.[1,2] Such flows are driven by buoyancy, but the physical mechanisms that limit the flow may be very different depending on the configuration and the type of fluid. While inertial forces are dominant for large-scale motions of a low viscosity fluid,[3,4] viscosity controls the flow of very viscous fluids at small thicknesses or inside a narrow channel. Such viscous flows have been studied experimentally and theoretically,[5–7] but often in weakly confined configurations (for instance a fluid spreading inside a thick layer of another fluid). Confinement is important in the lock-exchange problem, which has been investigated both in horizontal[8,9] and sloping[10] channels. Inertia, however, dominates in most studies performed in this configuration.

The present work studies the different regimes observed during the relative interpenetration of two fluids of different densities but the same viscosity. The fluids start in an unstable configuration in the confined geometry of a long nearly horizontal tube. The study focuses on the transient regimes observed before the velocity of the front becomes constant and on the relative influence of the inertial and viscous effects.

In previous papers,[11–13] we studied the stationary regimes for tubes at different angles α to the horizontal, for different density contrasts between the two fluids, and different values of their common viscosity. For tubes close to vertical ($\alpha \to 90°$), one observes weak turbulent mixing and the velocity of the front V_f increases as the tube is tilted away from vertical. When α decreases further, V_f reaches an upper limiting value V_f^M which is almost constant with α and which is controlled by inertia.[12] In this case, mixing is much less efficient than in the first regime. Then, as $\alpha \to 0$, V_f decreases to very low values. In this latter regime, there is a Poiseuille-like counterflow of the two fluids and viscous forces dominate. The present paper deals exclusively with the two regimes in which the tube is close to horizontal with little or no mixing.

After discussing the experimental setup and procedure in Sec. II, the key characteristic velocities of the problem (inertial and viscous) will be introduced in Sec. III. This allows us to suggest and test scaling laws. Then, the different regimes of the motion of the front observed at early times will be identified qualitatively in Sec. IV. A simple approximate model will be developed to account for them in Sec. V and compared with the experimental data in Sec. VI. Finally, a more elaborate model in Sec. VII allows us to predict both the concentration profiles and the velocity of the front both in the transient and stationary regimes: it will be applied to horizontal and tilted tubes.

II. EXPERIMENTAL SETUP

The experiments are realized in a 3.5-m-long transparent tube with a $d=20$ mm internal diameter which can be split into two isolated parts by a gate valve located at the half length (Fig. 1). The lower half of the tube is initially filled

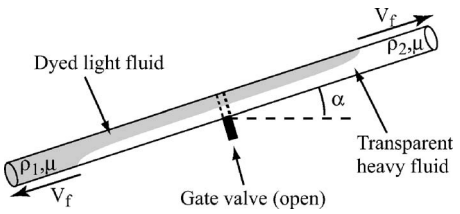

FIG. 1. Experimental setup.

with a light dyed fluid (nigrosin-water solution of density ρ_1) and the upper one by a heavy transparent fluid (salt-water solution of density ρ_2). The density contrast between the fluids is characterized by the Atwood number $\mathrm{At}=(\rho_2-\rho_1)/(\rho_2+\rho_1)$, where At ranges between 10^{-3} and 4×10^{-2}. The dynamic viscosities μ of the two fluids are equal and different solutions with $10^{-3}\leqslant\mu\leqslant4\times10^{-3}$ Pa s have been used. The tube is closed at both ends so that, in order to conserve mass, the upward flow of light fluid is compensated by a downward flow of heavy fluid; the Atwood number At is low enough so that the Boussinesq approximation is valid and the flows of both fluids are symmetrical. In the first series of experiments, the tube is illuminated from the back and, at the initial time, the gate valve is opened and images of flow in the tube are recorded at regular time intervals. Video recordings are also realized to examine local, fast motions of the fluids during the flow. The front velocity V_f is determined directly from its displacement between successive images.

III. CHARACTERISTIC VELOCITIES IN THE STATIONARY FLOW REGIMES

When no turbulence is present, the flow is nearly parallel in the bulk of the fluid outside the vicinity of the upper and lower fronts (Fig. 1): inertial terms are negligible in the equation of motion of the two fluids, and a Poiseuille-like developed flow is observed. Then, buoyancy forces $\sim(\rho_2-\rho_1)g$ are balanced by viscous forces scaling like $\mu V/d^2$, allowing one to define a characteristic velocity,

$$V_\nu=\frac{\mathrm{At}\,gd^2}{\nu},\tag{1}$$

where ν is defined as $2\mu/(\rho_2+\rho_1)$. Actually, for a counterflow parallel to the tube axis, the driving force is associated to the longitudinal gravity component $g\sin\alpha$ so that the relevant characteristic viscous velocity is $V_\nu\sin\alpha$.

Near to the front, the flow can no longer be considered as quasiparallel: inertial terms resulting from three-dimensional effects are then dominant (the Reynolds number is generally $\gg1$). Viscous forces are localized in a boundary layer close to the interface: the outside flow may therefore be considered as potential in this region. In this case, velocity variations between the tip of the front and its side (where the interface is nearly parallel to the tube axis) result in Bernoulli pressure differences of the order of ρV^2. These will be compensated by hydrostatic pressure differences that are

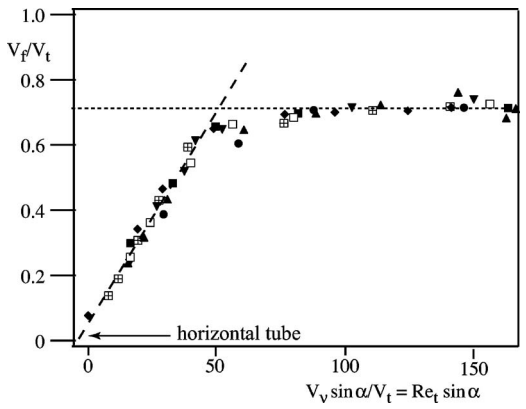

FIG. 2. Variation of the normalized stationary front velocity V_f/V_t as a function of the normalized characteristic viscous velocity $V_\nu\sin\alpha/V_t$ $(=\mathrm{Re}_t\sin\alpha)$. Data correspond to different tilt angles $(0\leqslant\alpha\leqslant30°)$ and to density contrasts: $\mathrm{At}=3.5\times10^{-2}$ (●), 10^{-2} (■), 4×10^{-3} (◆), 10^{-3} (▼), and 4×10^{-4} (▲) with $\mu=10^{-3}$ Pa s and to viscosities $\mu=10^{-3}$ Pa s (■), 4×10^{-3} Pa s (⊞) with $\mathrm{At}=10^{-2}$. Dotted line: $V_f=0.7V_t$; dashed line: $V_f=0.0145V_\nu\sin\alpha$ [see Eq. (10)].

of the order of $(\rho_2-\rho_1)gd$ (the vertical size of the front is of the order of d for all values of α). This suggests the introduction of a characteristic inertial velocity,

$$V_t=\sqrt{\mathrm{At}\,gd}.\tag{2}$$

Using V_t and d as the characteristic velocity and length scales allows one to define the characteristic Reynolds number,

$$\mathrm{Re}_t=\frac{V_td}{\nu}=\sqrt{\frac{\mathrm{At}\,gd^3}{\nu^2}}=\frac{V_\nu}{V_t}.\tag{3}$$

One defines also a second Reynolds number $\mathrm{Re}_\nu=V_\nu d/\nu$ $(=\mathrm{Re}_t^2)$ based on the characteristic viscous velocity.

The relevance of the characteristic velocities V_t and V_ν is checked by plotting in Fig. 2 the normalized stationary front velocity V_f/V_t as a function of the ratio $V_\nu\sin\alpha/V_t=\mathrm{Re}_t\sin\alpha$.[12] The values plotted in Fig. 2 have been determined from the displacement of the front measured at long times (but before reaching the ends of the tube). It will be seen below that they are an overestimation for low tilt angles α but that they represent, however, a good approximation. All data points in the figure correspond to the two flow regimes observed close to horizontal and for which there is little or no mixing between the fluids.

For $\mathrm{Re}_t\sin\alpha<50$, all data points corresponding to different values of At, ν, and α (see caption) collapse onto a single linear variation $(V_f\simeq0.0145\ V_\nu\sin\alpha)$ with a proportionality constant independent of the control variables. The relevant characteristic velocity for $\mathrm{Re}_t\sin\alpha<50$ is therefore V_ν, implying that the front velocity is controlled by viscous dissipation in the bulk of the fluid.

For $\mathrm{Re}_t\sin\alpha>50$, the points are close to a horizontal line corresponding to $V_f^M=0.7V_t$. The relevant characteristic velocity is therefore V_t in this domain, where it has been shown[13] that mixing is weak and that the density contrast at the front is equal to the imposed density difference of the unmixed fluids.

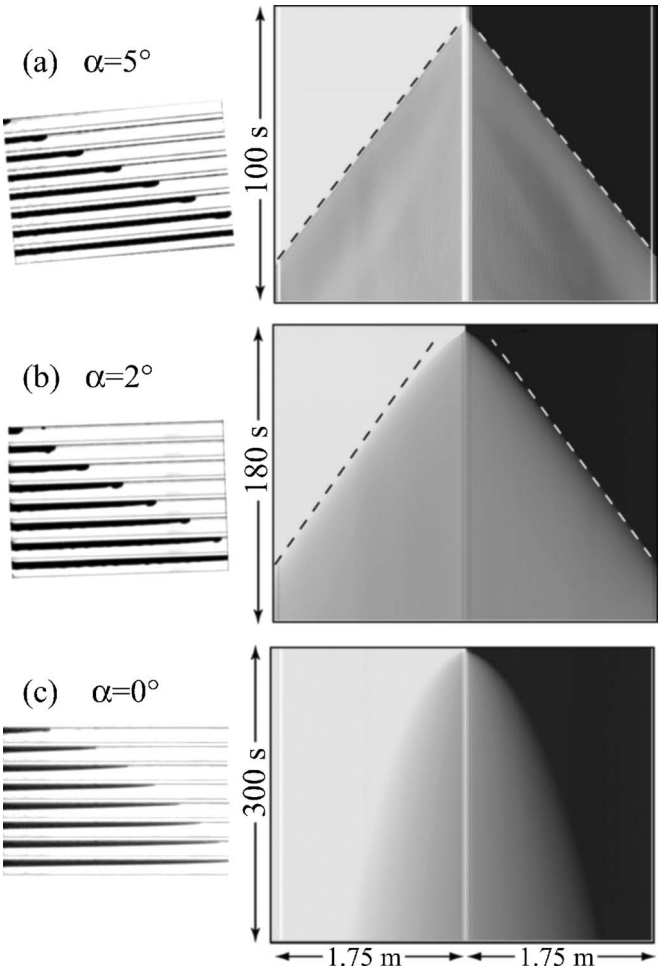

FIG. 3. Right: spatiotemporal diagrams of the average concentration variations (gray levels) along the tube for (a) $\alpha=5°$, (b) $\alpha=2°$, and (c) $\alpha=0°$ with $\mathrm{At}=3.9\times10^{-3}$, $\nu=10^{-6}$ m^2/s, $d=20$ mm (corresponding values of $\mathrm{Re}_t \sin\alpha$: 48.5, 19.5, 0). Vertical scale: time; horizontal scale: distance along the tube. Dashed lines have slopes equal to velocities estimated for the stationary regime. Left: sequences of views of the tube for a flow regime corresponding to the spatiotemporal diagram.

The next sections of the paper are devoted to the study of transient flows both in the viscous regime and the first part of the "plateau" inertial regime.

IV. QUALITATIVE OBSERVATIONS OF THE TRANSIENT REGIMES AT EARLY TIMES

A qualitative view of the occurrence and duration of transient regimes is provided by the spatiotemporal diagrams displayed in Fig. 3: they correspond to three different tilt angles α between 0° and 5° but with the same values of At, d, and μ. Sequences of views of the tube obtained at early times during the same experiments are displayed on the left of the figure. In all cases, there is almost no mixing between the fluids and the angle of the pseudo-interface (i.e., the apparent interface between the miscible fluids while the mixing is negligible) with the tube axis is very small, except near the front. Therefore, the quasiparallel flow approximation is valid in between the fronts. In the images corresponding to $\alpha=2°$ and 5°, one observes a bump at the front (barely visible for $\alpha=0°$) that results from the inertial effects discussed in the preceding section. On the side of the bump where the velocity is highest, there is a larger Bernoulli pressure drop than at the tip of the front, which is a stagnation point. This is compensated by the hydrostatic pressure term due to the locally larger thickness of the bump of the interface (when the velocity is of the order of the characteristic velocity V_t discussed above, this thickness is of the order of d).

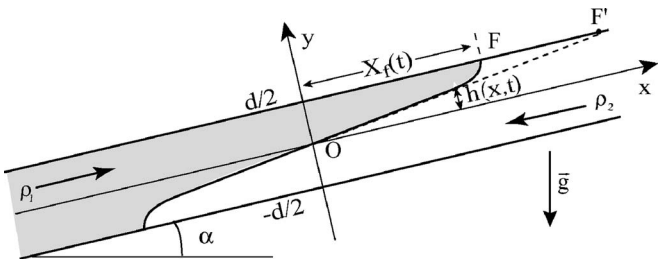

FIG. 4. Schematic view of the viscous counterflow of the fluids in the transient regime.

The instantaneous front velocities are determined in the spatiotemporal diagrams from the local slope of the boundaries separating the gray regions of the diagram (interpenetration zones) from the white and black regions (pure transparent and dyed fluid). It is observed that the boundaries corresponding to the rising and falling fronts have equal slopes so that the two front velocities are the same. All three experiments are within the range $0<\mathrm{Re}_t \sin\alpha<50$ estimated in the preceding section for obtaining a viscous regime at long times. Experiment (a) corresponding to $\alpha=5°$ is close to the limit with the inertial regime ($\mathrm{Re}_t \sin\alpha=48.5$). In this case, as well as at higher angles α, the boundaries marking the front displacement are straight (dashed lines) so that the front velocity is constant during the experiment.

For the horizontal tube ($\alpha=0°$), the front velocity V_f (as estimated from the slope of the boundary) decreases steadily with time, case (c). In the intermediate case (b) ($\alpha=2°$), V_f decreases at first but reaches a constant value at longer times (dashed line). The duration of the transient regime increases, therefore, when the tube is closer to horizontal.

V. TRANSIENT VISCOUS REGIME IN HORIZONTAL AND TILTED TUBES

A. Simple model of the transient viscous regime

In this section, an approximate relation is derived to estimate the variations of the front velocity V_f with time. A more complete approach will be used in Sec. VII to determine the full interface profile.

Figure 4 displays schematically the distribution of the two fluids in the vertical diametrical plane of the tube. Flow results from the combination of the effects of the components of gravity parallel and perpendicular to the tube axis. The transverse gravity component $g\cos\alpha$ is only effective when the interface between the two fluids is tilted with respect to the tube axis (i.e., if $\partial h/\partial x\neq0$ in Fig. 4). The axial gravity component $g\sin\alpha$ remains effective even when the interface is nearly parallel to the tube axis at very long times. However, it vanishes for horizontal tubes. In the following, the flow is assumed to be quasiparallel to the tube axis so

that transverse pressure gradients reflect only hydrostatic pressure variations. This assumption is valid if the local slope $\partial h/\partial x$ of the interface is small enough; this is not the case at short times, right after the opening of the valve. Writing the pressure difference between two nearby points of the interface and taking into account the continuity of pressure across the interface leads to

$$(\rho_2-\rho_1)g\cos\alpha\frac{\partial h}{\partial x}=-\left(\frac{\partial P_1}{\partial x}-\frac{\partial P_2}{\partial x}\right), \tag{4}$$

$$\mu\Delta v_{xi}=\frac{\partial P_i}{\partial x}+\rho_i g\sin\alpha \quad (i=1,2). \tag{5}$$

Flow results, therefore, from a combination of longitudinal pressure gradients proportional to $g\cos\alpha\partial h/\partial x$ [Eq. (4)] and longitudinal components of gravity proportional to $g\sin\alpha$.

Dimensionally, integrating Eq. (5) in the tube section $x=0$, corresponding to the gate valve, and where $h=0$, must lead to expressions of the following type for the mean velocities v_{x1}^m and v_{x2}^m:

$$v_{x1}^m=-\frac{F(0)d^2}{\mu}\left(\frac{\partial P_1}{\partial x}+\rho_1 g\sin\alpha\right),$$
$$v_{x2}^m=-\frac{F(0)d^2}{\mu}\left(\frac{\partial P_2}{\partial x}+\rho_2 g\sin\alpha\right). \tag{6}$$

The coefficient $F(0)$ is the same in both relations due to the symmetry of the equations and of the flow geometry. This symmetry also allows one to compute $F(0)$ analytically[12] with

$$F(0)=\frac{1}{16}-\frac{1}{2\pi^2}\simeq 0.0118. \tag{7}$$

The volume flow rates Q_1 and Q_2 are equal and opposite in all tube sections to ensure mass conservation so that, for $x=0$, $v_{x1}^m=-v_{x2}^m=v_{\mathrm{visc}}$ (the areas occupied by the two fluids have the same value $\pi d^2/8$). The common value v_{visc} of the two velocities is computed by combining Eqs. (4) and (6),

$$v_{\mathrm{visc}}=F(0)\frac{\mathrm{At}\,gd^2}{\nu}\sin\alpha\left(1+\frac{\partial h}{\partial x}\cot\alpha\right). \tag{8}$$

At long times, the slope of the interface decreases to zero and the second term of Eq. (8) is negligible: from Eqs. (1) and (8), v_{visc} is then equal to

$$v_{\mathrm{visc}}^{\infty}=F(0)\frac{\mathrm{At}\,gd^2}{\nu}\sin\alpha=F(0)V_\nu\sin\alpha. \tag{9}$$

This value will represent in the following a convenient reference velocity. The front velocity $V_f=dX_f/dt$ may be expected to follow the same scaling laws as v_{visc} (mass conservation would require that these velocities be equal if h remained equal to zero up to the front). We assume, therefore, that the limiting velocity V_f^{∞} satisfies

$$V_f^{\infty}=k_\nu V_\nu\sin\alpha, \tag{10}$$

in which k_ν is a coefficient of the same order as $F(0)$ (but generally different). Assuming that the dependence of V_f on the slope of the interface is the same as that of v_{visc}, Eq. (8) leads to

$$V_f=V_f^{\infty}\left(1+\frac{\partial h}{\partial x}\cot\alpha\right). \tag{11}$$

In the special case of horizontal tubes, the expression of v_{visc} is obtained by combining Eqs. (4) and (6),

$$v_{\mathrm{visc}}=F(0)V_\nu\frac{\partial h}{\partial x}, \tag{12}$$

and V_f is assumed to obey the similar relation,

$$V_f=k_\nu V_\nu\frac{\partial h}{\partial x}. \tag{13}$$

The following expression of the slope $\partial h/\partial x$ is assumed to analyze the variations of the flow velocity with time:

$$\frac{\partial h}{\partial x}=\lambda\frac{d}{2X_f}, \tag{14}$$

in which X_f is the distance of the front from the gate valve and $\lambda\leqslant 1$ is equal to the ratio of the coordinates along the x axis of points F and F' in Fig. 4; the coefficient λ is, for simplicity, assumed to remain constant during the experiment.

Finally, for $\alpha\neq 0°$,

$$V_f=\frac{dX_f}{dt}=k_\nu V_\nu\sin\alpha\left(1+\lambda\cot\alpha\frac{d}{2X_f}\right), \tag{15}$$

and, for $\alpha=0°$,

$$V_f=\frac{dX_f}{dt}=k_\nu\lambda V_\nu\frac{d}{2X_f}. \tag{16}$$

B. Front velocity variations with time at different tilt angles

Figures 5(a)–5(c) display variations of V_f as a function of the distance X_f predicted by Eqs. (15) and (16). At short times, Eqs. (15) and (16) predict a divergence of the velocity of the viscous flow. This is not physically acceptable and V_f will be limited by inertial effects right at the front (see the above discussion); it will then be of the order of the characteristic inertial velocity V_t with $V_f=k_iV_t$. Note that, right after the opening of the valve, the fluid accelerates briefly until the inertial velocity k_iV_t is reached. This phase of the front motion is, however, too short to be studied precisely experimentally here.

Three different cases are finally expected in our experiments.

(a): $\alpha\neq 0°$, $k_iV_t\leqslant k_\nu V_\nu\sin\alpha$ [Fig. 5(b)]: the velocity v_{visc} remains always larger than the inertial velocity k_iV_t. The front velocity is then always determined by inertial effects and equal to k_iV_t.

(b): $\alpha\neq 0°$, $k_iV_t>k_\nu V_\nu\sin\alpha$ [Fig. 5(b)]: the front velocity V_f is equal to k_iV_t at short times until the velocity v_{visc} from Eq. (15) is lower than k_iV_t. Then, the front velocity is limited by viscous dissipation in the whole flow

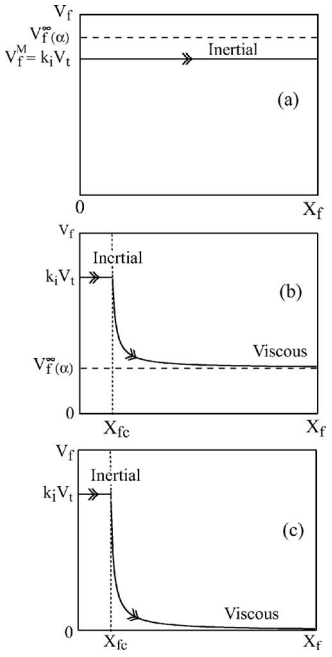

FIG. 5. Front velocity variation as a function of distance X_f from the gate valve (continuous line). (a) $\alpha \neq 0°$: $k_i V_t \leq k_\nu V_\nu \sin \alpha$. (b) $\alpha \neq 0°$: $k_i V_t > k_\nu V_\nu \sin \alpha$. (c) $\alpha = 0°$. Dashed line: $k_\nu V_\nu \sin \alpha$. Dotted line: $X_f = X_{fc}$. Arrows: trend of the evolution of the velocity with time.

and the front velocity decreases down to the limiting value, $V_f = k_\nu V_\nu \sin \alpha$ following Eq. (15).

(c): $\alpha = 0°$, $k_i V_t > k_\nu V_\nu \sin \alpha$ [Fig. 5(c)]: the results are the same as in the previous case, except that the limiting velocity at long times is zero.

C. Domains of existence of the different flow regimes

The discussion of the previous part implies that the dynamics of the front remains inertial at all times if the inertial velocity $k_i V_t$ is lower than the limiting viscous velocity $k_\nu V_\nu \sin \alpha$. The transition toward a regime in which the dynamics is viscous at long times takes place when these two velocities are equal, i.e., at a critical tilt angle α_c such that

$$\sin \alpha_c = \frac{k_i}{k_\nu} \frac{V_t}{V_\nu} = \frac{1}{\mathrm{Re}_t} \frac{k_i}{k_\nu}. \tag{17}$$

Using the values of k_i and k_ν deduced below from the experiments leads to a value of $\mathrm{Re}_t \sin \alpha_c$ of the order of 50 in good agreement with the transition value in Fig. 2. As could be expected, the angle α_c decreases when the inertial Reynolds number Re_t increases. For $\alpha < \alpha_c$, the front dynamics becomes controlled by viscosity when the distance X_f is larger than the transition value X_{fc} at which v_{visc} is equal to the inertial velocity $k_i V_t$. The distance X_{fc} should then satisfy

$$\frac{X_{fc}}{d} = \frac{\lambda \cos \alpha}{2(\sin \alpha_c - \sin \alpha)}. \tag{18}$$

The variation with α of the distance X_{fc} at which the transition takes place is displayed in Fig. 6 for fixed values of the parameters d, ν, At, and for $\lambda = 1$ (continuous line). The vertical dashed line marks the critical angle $\alpha = \alpha_c$: one observes

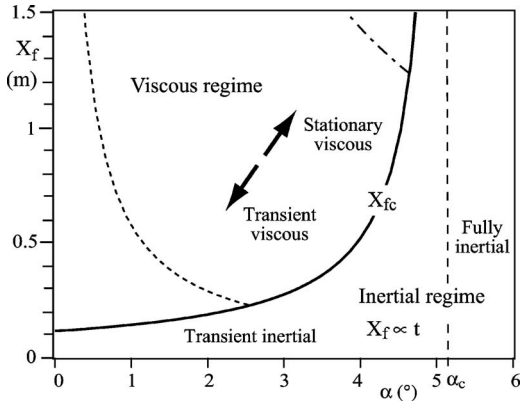

FIG. 6. Map of regimes observed as a function of tilt angle α and distance X_f of the front from the gate valve. Control parameter values: At=3.9 $\times 10^{-3}$, d=20 mm, $\nu = 10^{-6}$ m^2/s, and λ=1. Continuous line: boundary between inertial and viscous regimes $[X_{fc}(\alpha)]$. Vertical dashed line: upper limiting angle for observing viscous regime. Dotted line: transient term in Eq. (15) equal to the stationary term. Dash-dotted line: transient term in Eq. (15) equal to 10% of the stationary term.

that X_{fc} diverges when α increases toward α_c.

The transition angle and distance also depend on the value of Re_t. As Re_t increases, the transition angle α_c becomes smaller, Eq. (17). At a given angle $0 < \alpha < \alpha_c$, V_f remains at first constant in the inertial regime and decreases toward the limiting value V_f^∞ after the viscous regime is reached (the transition distance X_{fc} increases with Re_t). The dotted and dash-dotted lines in the figure are guides for the eye: they represent, for each tilt angle, the distance at which the contribution of transient effects represents, respectively, 100% and 10% of the stationary term. The distance necessary to reach the limiting velocity with a good approximation increases, therefore, significantly when $\alpha \to 0$. More specifically, after a distance X_f=1.5 m (half the tube length), the transient term still represents a relative correction of more than 10% for $\alpha < 4°$. This implies that the values of V_f^∞ that were directly determined from the spatiotemporal diagrams may be overestimated so that a more precise determination taking into account the transient effects is necessary. When $\alpha = 0$ (horizontal tube), the limiting velocity is zero and the motion always appears as transient.

VI. COMPARISON WITH EXPERIMENTAL DATA

A. Initial inertial regime

Two limiting examples of the occurrence of inertial regimes are displayed in Fig. 7.

For $\alpha = 0°$, a transition between two regimes in which the distance X_f is, respectively, proportional to t and $t^{1/2}$ is clearly visible in log-log coordinates (inset). At early times, the velocity is limited by inertial effects and has a constant value $k_i V_t$ with $X_f \propto t$; then, as viscosity becomes dominant, the velocity decreases toward zero with $X_f \propto t^{1/2}$ as predicted in Fig. 5(c).

For $\alpha = 4°$, and with the same values of At, d, and ν, X_f increases linearly with t at all distances investigated (main plot of Figs. 7 and 9): at this tilt angle, very close to the critical value α_c, the transition toward the viscous regime

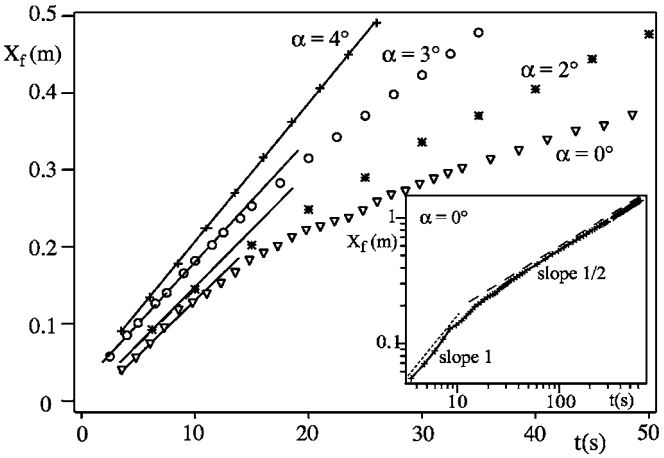

FIG. 7. Variation of the distance X_f of the front from the gate valve with the time t (At=3.9×10^{-3}, d=20 mm, $\nu=10^{-6}$ m^2/s). Lines: fit of data points corresponding to early times by a linear variation (continuous lines). (▽): α=0°; (∗): α=2°; (○): α=3°: (+): α=4°. For clarity, the different curves have been shifted upward relative to each other by a distance increasing with α. Inset: variation of X_f with time for α=0 in log-log coordinates (no shift has been introduced on the values of X_f).

would take place at distances beyond the experimental range so that the slope of the curve reflects solely the transient inertial regime. A similar linear increase of X_f with t is also observed at higher angles α.

At intermediate angles ($0°<\alpha<4°$), X_f increases at first linearly with the time t in the inertial regime (Fig. 7); then, a downward curvature appears after the transition toward the viscous regime. The inertial velocity k_i V_t in the linear region is determined by a linear fit on the variation of X_f: the variation with α of values of $k_i=V_f/V_t$ deduced in this way is displayed in Fig. 8.

The coefficient k_i increases at first roughly linearly from $k_i\simeq0.5$ for α=0° up to $k_i\simeq0.65$ for α=5° and then levels off toward a value $k_i\simeq0.7$ for $\alpha\simeq10°$. The variation near α =0° may reflect the lesser amount of buoyant energy available to compensate for the viscous dissipation.

Regarding the transition from the inertial to the viscous regime, the distance X_f corresponding to this transition may be detected from the onset of deviations from

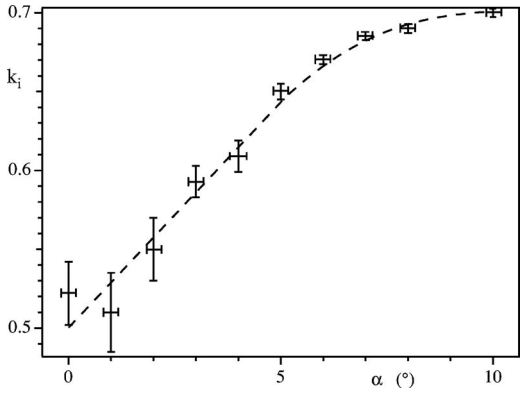

FIG. 8. Variation of the coefficient k_i characterizing the front velocity in the inertial regime as a function of the tilt angle α (At=3.9×10^{-3}, d=20 mm, $\nu=10^{-6}$ m^2/s). The dashed line is a guide for the eye; horizontal and vertical lines on the data points indicate the error bars.

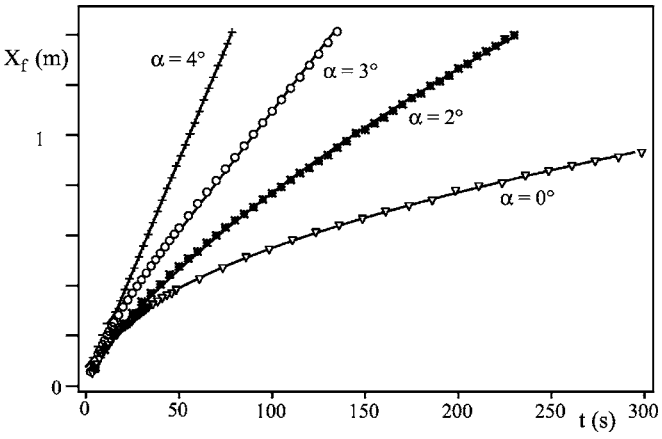

FIG. 9. Front displacement X_f as a function of elapsed time t for different tilt angles α (At=3.9×10^{-3}, d=20 mm, and $\nu=10^{-6}$ m^2/s). Symbols: experimental points. Lines: fitted curves obtained using Eqs. (19) and (20). (▽): α=0°; (∗): α=1°; (○): α=2°; (+): α=5°.

the linear variation. The corresponding distances have been compared with transition distances estimated from the diagram of Fig. 6. The transitions take place on the experimental curves of Fig. 7, respectively, for $X_f=0.4\pm0.1$ m(4°), $X_f=0.33\pm0.03$ m(3°), $X_f=0.23\pm0.03$ m(2°), and $X_f\simeq0.125\pm0.05$ m(0°) in good agreement with the respective theoretical values X_f=0.5 m, X_f=0.3 m, X_f=0.2 m, and X_f=0.12 m. For α=4°, the transition is poorly defined due to the vicinity of α_c.

B. Viscous regime

Figure 9 displays the same experimental variation of the distance X_f with the time t for different tilt angles α (Fig. 7 is actually a zoomed view of the same data at early times while Fig. 9 corresponds to the full range of distances over which the front displacement has been measured). Qualitatively, X_f increases faster with t at larger tilt angles α. Also, the transient phase before the viscous stationary regime is reached is shorter and shorter as α increases. These experimental curves have been fitted by the following theoretical variations obtained by integrating analytically Eqs. (15) and (16) with respect to X_f (continuous lines):

$$t=\frac{1}{k_\nu V_\nu \sin\alpha}\left[X_f-\frac{\lambda d\cot\alpha}{2}\ln\left(1+\frac{2X_f}{\lambda d\cot\alpha}\right)\right]+\text{const}, \tag{19}$$

valid for $\alpha\neq0°$ and

$$t=\frac{1}{k_\nu V_\nu \lambda}\frac{X_f^2}{d}+\text{const}, \tag{20}$$

valid for α=0°. In these fits, λ (assumed to be constant with time), k_ν, and the integration constant are the adjustable parameters while V_ν, α, and d are known.

Equation (20) accounts for the variation of X_f as $t^{1/2}$ at long times for horizontal tubes (inset of Fig. 7). Other values of the exponent have been reported for viscous spreading on

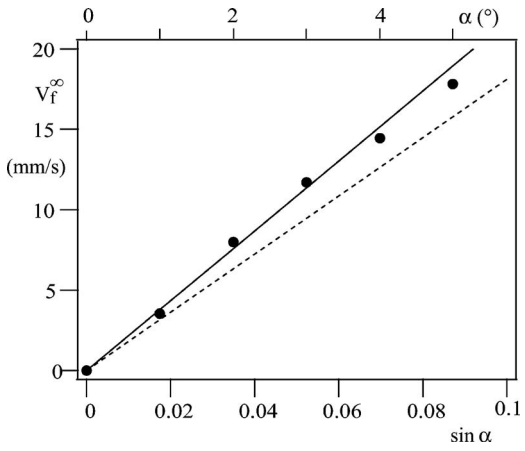

FIG. 10. Variation of the stationary front velocities as a function of sin α (At=3.9×10^{-3}, d=20 mm, and $\nu=10^{-6}$ m^2/s). Black circles: experimental values estimated from the fits of Fig. 9. Dotted line: estimation of stationary front velocity assuming $V_f^\infty=v_{\mathrm{visc}}^\infty$ [Eq. (9)]. Continuous line: estimation from Eq. (35) derived theoretically in Sec. VII C.

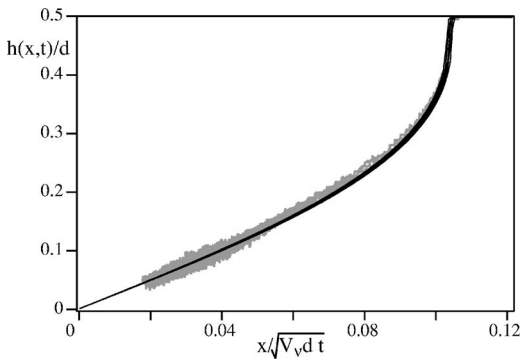

FIG. 11. Gray lines: overlay of normalized front profiles $h(x,t)/d$ determined at intervals Δt=25 s by the LIF technique as a function of the normalized distance $x/(V_\nu dt)^{1/2}$ from the gate valve (continuous gray curves). Times have been shifted by a constant small amount (10 s) reflecting experimental delays in order to obtain an optimal collapse. Continuous dark lines: theoretical profiles corresponding to different times determined by a numerical integration of Eq. (27). Later times correspond to the rightmost curve. The horizontal scale for the experimental data has been adjusted so that the experimental and theoretical displacements with time of the front tip coincide.

horizontal planes[7] but in different configurations; three-dimensional simulations in the same geometry as the present one do provide values of the order of 0.5.[14]

The good fits displayed in Fig. 9 for the full range of tilt angles investigated indicate that the assumption of a value of the coefficient λ constant with time is reasonable for fitting purposes. The fitted value of λ decreases from λ=0.7 for $\alpha=0°$ to λ=0 for $\alpha=5°$: this reflects an increasing magnitude of the inertial effects at the front, resulting in a higher height of the interface right behind the front and, therefore, in a reduced slope of the upstream profile.

The key feature of these fits is the fact that they provide a precise value of the coefficient k_ν even if the stationary limiting velocity cannot be reached during the experiment. Using this procedure allows one to take into account the influence of the logarithmic term in Eq. (19), which may remain significant for a long distance and induce errors in the front velocity measurement.

The velocities $V_f^\infty=k_\nu V_\nu \sin\alpha$ [Eq. (10)] deduced from these values of k_ν are plotted in Fig. 10 as a function of sin α. The variation of V_f^∞ with sin α is precisely linear as expected, which implies that k_ν is nearly constant with α. For $\alpha=5° \simeq \alpha_c$, the value of V_f^∞ is slightly lower than the linear trend, implying that inertial forces already slow down the front. As a reference, the variation of the velocity $v_{\mathrm{visc}}^\infty(\alpha)$ [Eq. (9)] is represented by the dotted line with $V_f^\infty \simeq 1.2\times v_{\mathrm{visc}}^\infty$. A more precise theoretical estimation will be provided in Sec. VII C.

Note that stationary front velocities plotted in Fig. 2 were directly estimated from the slope of the features marking the front motion in the spatiotemporal diagrams. These estimations may be higher (by a few percent) than those plotted in Fig. 10 because the front motion was not yet stationary, due to the large relative influence of the logarithmic term of Eq. (19).

VII. VISCOUS SPREADING OF THE PSEUDO-INTERFACES

A. Experimental pseudo-interface profiles in horizontal tubes

Up to now, only front velocity variations have been discussed, both for α equal to and higher than 0°, since it is the most precise measurement available. However, in these weak mixing regimes, it is also possible to determine the profile of the "pseudo-interface" of the fluids by using a fluorescent dye and illuminating a vertical diametrical plane of the tube by a thin plane laser light sheet. The use of this so-called LIF technique in the present experiment has been described in Ref. 13. To reduce optical distortion, the tube is enclosed in a water-filled cell with a square cross section: for practical reasons, the domain of observation (entirely within the upper half of the tube length) is 0.8 m long and the minimum useful distance from the gate valve is 0.3 m. This method provides an excellent contrast between the two fluids, and their pseudo-interface is determined easily by a thresholding technique.

This procedure has been applied to horizontal tubes in which the pseudo-interface is particularly sharp. This case is also of special interest since, in the viscous regime, the front displacement has been found to satisfy a well defined scaling law $X_f \propto t^{1/2}$. To verify whether the profile $h(x,t)$ displays similar properties, the normalized front profile in the vertical diametrical plane is plotted in Fig. 11 as a function of the reduced distance $x/(V_\nu dt)^{1/2}$ (only the upper halves of the tube length and of its diameter appear in the figure). Profiles corresponding to different times have been superimposed (gray lines) and an excellent collapse of all curves is observed (note that the distance of the observation window from the front varies from one profile to another). The experimental curve does not extend down to $x/(V_\nu dt)^{1/2}=0$

due to the limited duration of the experiments and to the finite distance between the gate valve and the measurement window.

This collapse demonstrates that the variation of the height $h(x,t)$ of the interface depends only on the variable $x/t^{1/2}$. However, although the profile spreads out as $t^{1/2}$ as for a diffusive process, it is not simply diffusive: more specifically, the profile is delimited by a well-defined front while the slope of simple diffusive profiles would decrease continuously with distance. Note that the self-similarity of the curves at long times is only satisfied for horizontal tubes $\alpha=0$. For $\alpha\neq 0$, additional terms appear (reflecting the nonzero final front velocity V_f^{∞}) and the profiles are no longer similar.

B. Modeling the interface profile in the horizontal tube

The notations will be the same as in Fig. 4 and one assumes that the flow velocity is quasiparallel and that the interface has a constant height in a section ($x=cst$) of the tube. The velocities v_{xi} must be continuous at the interface (as well as the viscous shear stresses) and vanish on the tube walls. Under these assumptions, Eqs. (4) and (5) remain valid, but Eq. (12) cannot be generalized since, for $X_f\neq 0$, the areas occupied by the two fluids and their absolute mean velocities are different. We shall use instead the flow rates Q_1 and Q_2 of the two fluids, which still satisfy $Q_1+Q_2=0$ in all tube sections so that

$$Q_1=-Q_2=F\left(\frac{h(x,t)}{d}\right)V_\nu\frac{\pi d^2}{8}\frac{\partial h}{\partial x}. \tag{21}$$

For $h(x,t)/d=0$, the two fluids occupy the same area $\pi d^2/8$; Eq. (21) is equivalent to Eq. (12) within a factor $\pi d^2/8$.

At other distances $x\neq 0$, the function $F(h/d)$ must be symmetrical with respect to 0 with $F(\pm 1/2)=0$ (one of the fluids disappears). Close to the walls ($h/d\to\pm 1/2$), $F(h/d)$ may be estimated analytically using the lubrication approximation when fluid 1 flows inside a thin layer (the thickness must be small compared with the transverse width of the interface). Since $Q_1=-Q_2$, the driving force for fluid 2 is negligible compared with that in fluid 1 (the same flow rate takes place in a much larger area). This implies, from Eqs. (4) and (5), that $\partial P_2/\partial x=0$ so that $\partial P_1/\partial x=(\rho_1-\rho_2)g\partial h/\partial x$. For the same reason, the shear stress in fluid 2, and therefore the velocity gradient, may be assumed to be zero: they will then also be zero in fluid 1 by continuity at the interface. Integrating across the width of this interface elementary local flow rates driven by the pressure gradient $\partial P_1/\partial x$ and assumed to take place between parallel planes provides the following expression of $F(h/d)$:

$$F\left(\frac{h(x,t)}{d}\right)=\frac{32\sqrt{2}}{105\pi}\left(1-\frac{2h}{d}\right)^{7/2}. \tag{22}$$

The 7/2 power combines the factors $(1-2h/d)^3$ and $(1-2h/d)^{1/2}$ reflecting, respectively, the influences of the thickness and of the width of the film of liquid 1 in the section $x=cst$. The flow rate Q_2 is computed for fluid 2 in the same way when $h\to -1/2$, leading to an identical relation, this time as a function of $1+2h/d$.

These two expressions may be combined into the following one:

$$F\left(\frac{h(x,t)}{d}\right)=\frac{4}{105\pi}\left(1-\frac{4h^2}{d^2}\right)^{7/2}. \tag{23}$$

Although these equations should only be valid if $h\to\pm 1/2$, the value obtained by taking $h=0$ in Eq. (23), i.e., 1.21×10^{-2}, is close the value of $F(0)$ from Eq. (7) (1.18×10^{-2}). This suggests to use the following empirical expression of F for all values of h:

$$F\left(\frac{h(x,t)}{d}\right)=F(0)\left(1-\frac{4h^2}{d^2}\right)^{7/2}. \tag{24}$$

To verify the validity of this expression, Eqs. (5) have been integrated numerically in the 2D section of the tube using a finite-difference method for different values of h, under the same assumptions as above regarding the boundary conditions. The results were in agreement to within better than 2.5% with Eq. (24), which is therefore used in the following to estimate Q_1 and Q_2.

The conservation of the mass of fluid 1 can be written as

$$\frac{\partial Q_1}{\partial x}=-\frac{dA_1}{dh}\frac{\partial h}{\partial t}=\sqrt{d^2-4h^2}\frac{\partial h}{\partial t}, \tag{25}$$

in which

$$A_1(h)=\frac{d^2}{4}\arccos\left(\frac{2h}{d}\right)-\frac{1}{2}h\sqrt{d^2-4h^2} \tag{26}$$

is the area occupied by fluid 1 in the tube section and $(d^2-4h^2)^{1/2}$ is the width of the interface in the tube section.

Combining Eqs. (21), (24), and (25) leads to the nonlinear diffusion equation satisfied by the local height $h(x,t)$ of the interface profile,

$$\frac{\partial h}{\partial t}=\frac{F(0)V_\nu\pi d}{8}\frac{1}{(1-4h^2/d^2)^{1/2}}\frac{\partial}{\partial x}\left[\left(1-\frac{4h^2}{d^2}\right)^{7/2}\frac{\partial h}{\partial x}\right]. \tag{27}$$

Equation (27) has been integrated numerically: at $t=0$, h was given values $h=-1/2$ and $1/2$, respectively, for $x<0$ and $x>0$, with sharp linear variation from $-1/2$ to $1/2$ near $x=0$. To avoid numerical divergence issues, the ratio $1/(1-4h^2/d^2)^{1/2}$ is replaced by $1/(1.0001-4h^2/d^2)^{1/2}$ [the result was independent of the actual (small) value of the shift from 1].

These theoretical variations of the dimensionless height h/d as a function of the normalized distance $x/(V_\nu dt)^{1/2}$ at different times have been added to Fig. 11 (dark lines): they converge toward a self-similar profile depending only on the reduced variable $x/t^{1/2}$.

These curves first allow one to determine the variation of the distance X_f with time: in the self-similar regime, the corresponding predicted value of the ratio $X_f/(V_\nu dt)^{1/2}$ is 0.1045. Experimentally, the proportionality constant between X_f and $t^{1/2}$ can be determined from such fits as that displayed in Fig. 9 for $\alpha=0°$. Several experiments have been per-

formed and the values obtained for the ratio $X_f/(V_\nu dt)^{1/2}$ agree with the theoretical one with a dispersion of ±7.5% (asymmetries of up to 10% have in particular been observed between the velocities of the upward and downward moving fronts). The measurement is, however, very sensitive to minor errors in the horizontality of the tube.

Moreover, after adjusting slightly the horizontal scale of the theoretical profiles so that the front tips coincide exactly (as in Fig. 11), the theoretical profiles are very similar to the experimental ones (gray lines). The sharp slope at the fronts is in particular well reproduced.

C. Modeling the interface profile in tilted tubes

Equation (27) is generalized by modifying Eq. (21) to include the effect of the longitudinal gravity component $g \sin \alpha$ and of the reduced transverse gravity $g \cos \alpha$. For a given value of h, $F(h)$ remains the same and only the factor describing the driving force needs to be modified so that Eq. (21) becomes

$$Q_1 = -Q_2 = F\left(\frac{h(x,t)}{d}\right) V_\nu \frac{\pi d^2}{8}\left(\cos\alpha \frac{\partial h}{\partial x} + \sin\alpha\right). \quad (28)$$

The mass conservation relation (25) remains unchanged and Eq. (27) becomes

$$\frac{\partial h}{\partial t} = \frac{F(0)V_\nu \pi d}{8} \frac{1}{(1-4h^2/d^2)^{1/2}} \times \frac{\partial}{\partial x}\left[\left(1-\frac{4h^2}{d^2}\right)^{7/2}\left(\cos\alpha \frac{\partial h}{\partial x} + \sin\alpha\right)\right]. \quad (29)$$

At long times when $\partial h/\partial x \ll \tan\alpha$, this reduces to the hyperbolic equation

$$\frac{\partial h}{\partial t} = -\sin\alpha F(0) V_\nu \frac{7\pi h}{2d}\left(1-\frac{4h^2}{d^2}\right)^2 \frac{\partial h}{\partial x}. \quad (30)$$

Each point of the interface corresponding to a given value of h moves then at a constant velocity,

$$V_K(h) = \sin\alpha F(0) V_\nu \frac{7\pi h}{2d}\left(1-\frac{4h^2}{d^2}\right)^2. \quad (31)$$

This kinematic velocity $V_K(h)$ has a maximum for $h=h_M = d/20^{1/2} < 0.5d$ (and a minimum at the symmetric point $-h_M$). The corresponding maximum velocity value is

$$V_{K_M} = F(0) V_\nu \sin\alpha \frac{28\pi}{25\sqrt{5}} \simeq 1.57 v^\infty_{\text{visc}}. \quad (32)$$

As a result of this appearance of a maximum, the profiles must be bounded by two symmetric shock waves moving in opposite directions. The velocity $V_S(h)$ of a shock of height h is given by conservation of mass as

$$V_S(h) = \frac{Q(h)}{A(h)}, \quad (33)$$

in which $Q(h)$ is given by Eq. (28) and $A(h)$ by Eq. (26). At long times such that Eq. (31) is valid in the vicinity of the front, the velocity $V_S(h)$ must be equal to $V_K(h)$ by continuity. The corresponding theoretical value of the shock velocity is

$$V_S^\infty = 1.165 v^\infty_{\text{visc}}, \quad (34)$$

which is very close to the experimental value.

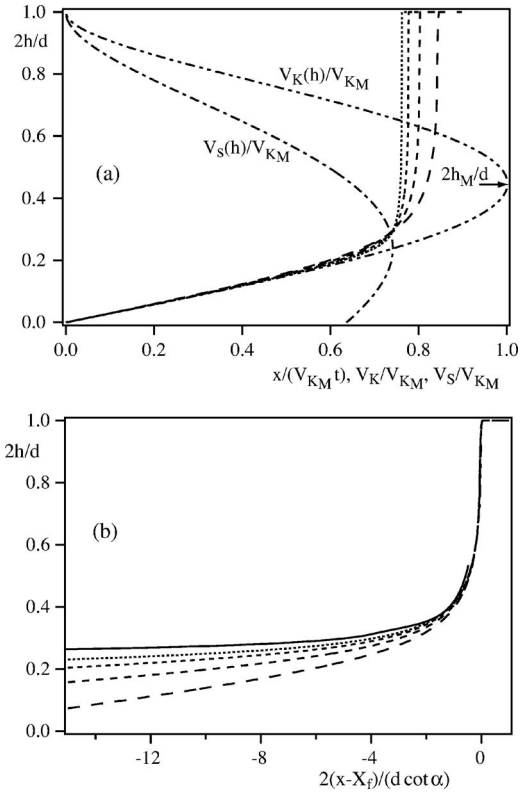

FIG. 12. (a) Numerical profiles $2h(x/t)/d$ of the interface as a function of $x/(V_{K_M}t)$ at different normalized times: $t=25,50,100,200$ (dashed lines with, respectively, decreasing dash lengths). Dash-dotted (dash-dot-dotted) line: variation of $2h/d$ as a function of the corresponding reduced shock wave velocity $V_S(h)/V_{K_M}$ from Eq. (33) [reduced theoretical kinematic interface velocity $V_K(h)/V_{K_M}$ from Eq. (31)] (b) Variation of $2h/d$ as a function of the normalized distance $2(x-X_f)/d\cot\alpha$ [same code as in (b) for the lengths of dashes]. Continuous line: theoretical stationary profile. Only parts of the profiles corresponding to $x \geqslant 0$ and $y \geqslant 0$ are shown.

To determine the profile of the interface, Eq. (29) has been integrated numerically: Figures 12(a) and 12(b) display profiles corresponding to different times. In Fig. 12(a), the scale of the distances has been normalized by $V_{K_M}t$ to allow one to compare the curves with the variation of the normalized kinematic wave velocity $V_K(h)/V_{K_M}$ (dash-dot-dotted line). The latter are in agreement with the numerical profiles in the rarefaction part of the curves up to values of $x/(V_{K_M}t)$ increasing slightly with time. Then h/d increases very sharply with $x/(V_{K_M}t)$ as expected for a shock front structure. The corresponding value of $x/(V_{K_M}t)$, which represents the location of the front, decreases as expected with time toward the theoretical value for which the curves $V_K(h)$ and $V_S(h)$ intersect.

The detailed structure of the front is shown in Fig. 12(b): it also displays the profiles of $h(x,t)/d$ at different times t but the horizontal scales are now not normalized by t but are shifted by a distance $X_f(t)$ such that the points corresponding to $2h/d=1$ coincide $\{2h[X_f(t)]/d=1\}$. The front part of the

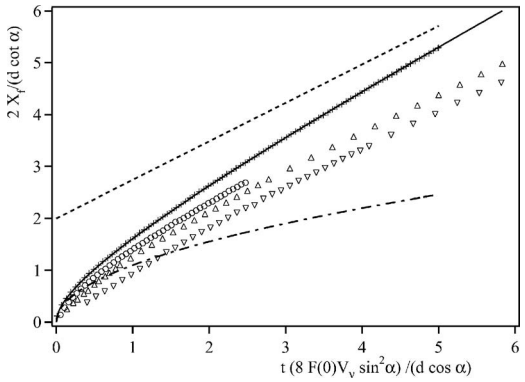

FIG. 13. Variation of the normalized front distance to the origin $2X_f/(d\cot\alpha)$ as a function of the normalized time $t(8k_\nu V_\nu \sin^2\alpha)/(d\cos\alpha)$. (+) Numerical data. Continuous line: fitted variation using Eq. (29). Experimental points (○): $\alpha=1°$, (△) $\alpha=2°$, (▽) $\alpha=3°$. Dash-dotted line: diffusive spreading at early times. Dotted line: limiting constant velocity motion at very long times.

different profiles corresponding to $2h/d \gtrsim 0.5$ also nearly coincide while the slope of the rear part decreases at longer times t. The global profile tends toward a limiting curve (continuous line) representing the solution of Eq. (29), which is stationary in the reference frame of the moving front. To compute this curve, the $\cos\alpha$ term is not neglected in Eq. (29). Note that the front appears very abrupt at long times in Fig. 12(a) only because the horizontal scale is normalized by time.

D. Experimental and theoretical front velocities in tilted tubes

To determine precisely the front velocity at different times and compare its variation with the experimental results, the displacement of the front with time is analyzed with the same method as the experiments. The displacement of the front is plotted as a function of time (Fig. 13) and fitted by Eq. (19) in order to estimate precisely the limiting velocity at long times. A very good fit of the equation (continuous line) with the numerical data (+ symbols) is obtained for a value $\lambda=0.77$ of the parameter relating the slope $\partial h/\partial x$ to the ratio $d/(2X_f)$. Taking into account the different normalization coefficients leads to the following relation between the front velocity V_f^∞ and the reference velocity $v_{\mathrm{visc}}^\infty = F(0)V_\nu \sin\alpha$ by

$$V_f^\infty = 1.165 v_{\mathrm{visc}}^\infty. \tag{35}$$

This theoretical variation is plotted in Fig. 10 (continuous line): the predicted slope coincides with that of the linear regression on the experimental data to better than 1%. This value coincides also with the theoretical estimation of Eq. (34). Regarding the transient front velocity variations, experimental data points corresponding to $\alpha=1°$, 2°, and 3° have been plotted for comparison in Fig. 13 with the same nondimensional variables as the numerical curve; no adjustable coefficient has been introduced. The experimental curve corresponding to $\alpha=1°$ is very close to the numerical one. The curves corresponding to $\alpha=2°$ and 3° follow the same trend at long times: however, they are shifted rightward and a constant velocity is reached earlier. The shift reflects in part the fact that, at early times, the front motion is controlled by inertia so that V_f is lower than the predictions of the model. These differences between the shapes of the curves are consistent with the fact that the fits of the experimental curves by Eq. (19) had provided values of the parameter λ decreasing with α and lower than the value $\lambda=0.77$ of the numerical model (except near $\alpha=0$). This discrepancy may reflect a residual influence of inertial effects at the front at early times, particularly near the transition to the inertial regime: different numerical initial conditions yielded different values for λ.

VIII. CONCLUSIONS

The experiments and theoretical models reported in the present paper have allowed us first to establish a criterion to discriminate between control by inertia or by viscosity of buoyancy-driven interpenetration flows in tubes slightly tilted from the horizontal. They have also allowed us to predict and analyze transient regimes such as initial flows controlled by inertia or variations with time of the velocities of viscous flows. These conclusions are valid at tilt angles α low enough so that mixing between the two fluids does not influence the front velocity.

For $\alpha < \alpha_c$ such that $\mathrm{Re}_t \sin\alpha_c \simeq 50$, the front velocity is initially determined by inertial effects at the front and, at later times, by viscous forces in the quasiparallel flow region between the two fronts. A similar transition from an inertial to a viscous regime has been discussed for $\alpha=0$ by Didden and Maxworthy in the case of unconfined gravity currents[6] and by Hoult for oil spreading on a liquid surface.[5]

Note that, even when inertia forces are negligible in the bulk of the flow, they often remain significant at the tip of the front where flow is three-dimensional. A feature reflecting these inertial effects is the bump-like structure at the front. As noted above, it results from the Bernoulli pressure drop on its upper side: the height of the bump increases, therefore, with the front velocity and becomes of the order of the tube diameter at the transition to the inertial regime. Another important result is the fact that, as Re_t increases, the distance X_{fc} necessary to reach the viscous regime increases.

Regarding the particular case of horizontal tubes, while X_{fc} decreases as $\alpha \to 0$ (Fig. 6), it does not vanish for $\alpha=0$. For horizontal tubes, therefore, and for large values of Re_t, the distance X_{fc} may be larger than the length of the experimental facilities (for $\alpha=0°$, X_{fc} varies as $k_\nu \mathrm{Re}_t d/k_i$). This explains why no viscous regime is reported either in horizontal lock-exchange experiments realized with low viscosity fluids and channel sections larger than in the present case[8,9] or in numerical simulations of such processes realized at high Re_t values.[4]

For tubes tilted with respect to the horizontal, the sine of the upper limiting angle $\sin(\alpha_c)$ for observing this viscous regime varies as the inverse of Re_t from Eq. (17). For instance, using this latter equation with $d=20$ mm, $\nu=10^{-6}$ m^2 s^{-1} (present experimental values) and $\sin(\alpha)\sim 1$, a viscous counterflow would only be observed for Atwood

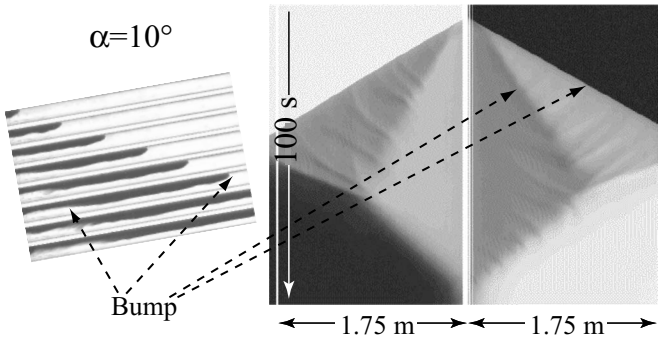

FIG. 14. Right: Spatiotemporal diagrams of the average concentration variations (gray levels) along the tube for $\alpha=10°$ with $\mathrm{At}=10^{-2}$, $\nu=2\times10^{-6}$ m^2/s, $d=20$ mm ($\mathrm{Re}_t \sin\alpha=80$). Vertical scale: time; horizontal scale: distance along the tube.—Left: sequence of views of the tube.

numbers At of the order of a few 10^{-5}. This is much lower than the typical density contrasts used in most experiments.

For $\alpha>\alpha_c$, the velocity V_f is always limited by inertial effects at the front and is constant except during the acceleration phase at very early times. This condition is, for instance, satisfied in the numerical simulations of Birman *et al.*[10] realized for $\alpha=40°$ and $\mathrm{Re}_t=2800$. These authors also do not observe a viscous regime in the horizontal case, likely due to the short path lengths that they can investigate [an estimation using Eq. (18) leads to $X_{fc}\simeq 30d$ while the maximum path length investigated is of the order of 10 times the channel depth].

Close to the transition angle, however, the flow in the remaining part of the tube still corresponds to a Poiseuille counterflow but with a mean velocity larger than that of the front. In contrast with the assumptions made up to now, a stationary flow regime cannot be attained: the incoming liquid accumulates behind the front and builds up a bump of increasing length visible in the sequence on the left of Fig. 14. The rear end of the bump moves downstream but at a slower velocity than that of the front (oblique line on the spatiotemporal diagram of Fig. 14).

Assuming that the flow rate is $Q_1(h_v)$ upstream of the bump [in which h_v is the local height of the interface and $Q_1(h)$ is given by Eq. (28)], the variation with time of the length $L(t)$ of the bump should satisfy, in order to ensure mass conservation,

$$\frac{dL}{dt}(A_{\mathrm{bump}}-A_v)=Q_1(h_v)-k_iV_fA_{\mathrm{bump}}. \tag{36}$$

The parameters A_{bump} and A_v are, respectively, the sections occupied by fluid 1 in the bump and upstream of it in the viscous flow region and A_v is assumed to remain constant with time. When α increases further above α_c, the viscous counterflow becomes unstable and turbulent dissipation slows down the flow between the fronts and adjusts the mean flow rate to the front velocity (until mixing becomes so efficient that the density contrast at the front is reduced—and, therefore, also V_f).[13]

Both the front velocity at long times and its transient behavior are well described quantitatively in the viscous regime by a model assuming quasiparallel Poiseuille flows, particularly when the tube is close to horizontal. The quantitative agreement is particularly good for the value of the velocity at long times. It should be remembered, however, that such a model cannot be strictly valid right at the front where the flow is no longer quasiparallel and inertial effects appear. Regarding the transient regime, the predictions of the model are good close to horizontal but the constant velocity is reached faster than expected as α increases and approaches the transition toward the inertial regime. The possible influence of inertial effects at the front may explain this discrepancy.

The interface profile along the tube is also predicted by the model: for a horizontal tube, the model predicts in particular the appearance of self-similar interface profiles depending only on the reduced variable $x/t^{1/2}$. This prediction is well verified by the experiment.

These results demonstrate that, particularly for systems of small size and small tilt angles with respect to the horizontal, the front and interface dynamics result from a subtle interplay between phenomena taking place over the full zone of coexistence of the two fluids and/or right at the front.

ACKNOWLEDGMENTS

We thank G. Chauvin and R. Pidoux for designing and realizing the experimental setup, and Y. Hallez and J. Magnaudet for helpful discussions.

[1] T. B. Benjamin, "Gravity currents and related phenomena," J. Fluid Mech. **31**, 209 (1968).
[2] J. E. Simpson, *Gravity Currents in the Environment and the Laboratory*, 2nd ed. (Cambridge University Press, Cambridge, UK, 1997).
[3] R. E. Britter and J. E. Simpson, "Experiments on the dynamics of a gravity current head," J. Fluid Mech. **88**, 223 (1978).
[4] C. Härtel, E. Meiburg, and F. Necker, "Analysis and numerical simulation of the flow at a gravity-current head. Part 1: Flow topology and front speed for slip and no-slip boundaries," J. Fluid Mech. **418**, 189 (2000).
[5] D. Hoult, "Oil spreading in the sea," Annu. Rev. Fluid Mech. **4**, 341 (1972).
[6] N. Didden and T. Maxworthy, "The viscous spreading of plane and axisymmetric gravity currents," J. Fluid Mech. **121**, 27 (1982).
[7] H. E. Huppert, "The propagation of two-dimensional and axisymmetric gravity currents over a rigid horizontal surface," J. Fluid Mech. **121**, 43 (1982).
[8] D. I. H. Barr, "Densimetric exchange flows in rectangular channels," Houille Blanche **22**, 619 (1967).
[9] J. O. Shin, S. B. Dalziel, and P. F. Linden, "Gravity currents produced by lock exchange," J. Fluid Mech. **521**, 1 (2004).
[10] V. K. Birman, B. A. Battandier, E. Meiburg, and P. F. Linden, "Lock-exchange flows in sloping channels," J. Fluid Mech. **53**, 1 (2007).
[11] T. Seon, J. P. Hulin, D. Salin, B. Perrin, and E. J. Hinch, "Buoyant mixing of miscible fluids in tilted tubes," Phys. Fluids **16**, L103 (2004).
[12] T. Seon, D. Salin, J. P. Hulin, B. Perrin, and E. J. Hinch, "Buoyancy driven front dynamics in tilted tubes," Phys. Fluids **17**, 031702 (2005).
[13] T. Seon, J. P. Hulin, D. Salin, B. Perrin, and E. J. Hinch, "LIF measurements of buoyancy driven mixing in tilted tubes," Phys. Fluids **18**, 041701 (2006).
[14] Y. Hallez and J. Magnaudet (private communication).